Online Microfluidic Production of Sustainable Cyrene™-Derived Porous Microparticles

Hassan El Itawi, Sami Fadlallah, Wichapol Leephakphumphanich, Nathalie Ruscassier, Aya Zoghlami, Florent Allais, Patrick Perré

To cite this version:

Hassan El Itawi, Sami Fadlallah, Wichapol Leephakphumphanich, Nathalie Ruscassier, Aya Zoghlami, et al.. Online Microfluidic Production of Sustainable Cyrene™-Derived Porous Microparticles. Sustainability, 2023, 15, ⟨10.3390/su15032023⟩. ⟨hal-03952238⟩

HAL Id: hal-03952238
https://hal.science/hal-03952238v1

Submitted on 23 Jan 2023

sustainability

MDPI

Article

Online Microfluidic Production of Sustainable Cyrene™-Derived Porous Microparticles

Hassan El Itawi [1,*], Sami Fadlallah [2,*], Wichapol Leephakphumphanich [1,2], Nathalie Ruscassier [3], Aya Zoghlami [1], Florent Allais [2] and Patrick Perré [1,3]

[1] Université Paris-Saclay, CentraleSupélec, Laboratoire de Génie des Procédés et Matériaux, Centre Européen de Biotechnologie et de Bioéconomie (CEBB), 3 Rue des Rouges Terres, 51110 Pomacle, France
[2] URD Agro-Biotechnologies Industrielles (ABI), CEBB, AgroParisTech, 51110 Pomacle, France
[3] Laboratoire de Génie des Procédés et Matériaux, Université Paris-Saclay, CentraleSupélec, 8–10 Rue Joliot-Curie, 91190 Gif-sur-Yvette, France
* Correspondence: hassan.el-itawi@centralesupelec.fr (H.E.I.); sami.fadlallah@agroparistech.fr (S.F.)

Abstract: The use of sustainable raw materials is now a necessity in all industries, including the production of porous microparticles. Cyrene™ is a cellulose-derived compound that is readily prepared through the reduction of the α,β-unsaturation of levoglucosenone (LGO)—a wood-based platform molecule. In this work, the importance of Cyrene™ as a potential bio-based molecule to produce sustainable porous microparticles is demonstrated. First, a methacrylic derivative of Cyrene™ (m-Cyrene) was synthesized. A microfluidic co-flow device was then established to produce m-Cyrene-based oil-in-water (O/W) controlled-size emulsions and to polymerize them by ultraviolet (UV) radiation in a vial. The continuous phase was a sodium dodecyl sulfate aqueous solution, and the dispersed phase was a mixture of m-Cyrene with methacrylic anhydride (MAN) at two different mass concentrations (i.e., 1 wt.% MAN and 92 wt.% MAN) and 2,2-dimethoxy-2-phenylacetophenone (DMPA) as a photoinitiator. The process used the lowest possible quantity of raw materials and avoided excessive purifications to produce homogeneous porous m-Cyrene-MAN microparticles. The controlled size and homogeneous size distribution of the produced polymer microparticles were confirmed by scanning electron microscope (SEM) images. The 3D microstructure as well as the porosity were determined using X-ray microtomography. The high-resolution 3D images produced indicate that the pores of the microparticles are homogeneous and that their porosity is controllable through the concentration of MAN in the monomer mixture (porosity of 30% for a 1 wt.% MAN ratio and 2% for a 92 wt.% MAN ratio). Such porosity control is very important for future potential encapsulation processes that require precise release control.

Keywords: sustainable production; size control; Cyrene™; microtomography; porosity

Citation: El Itawi, H.; Fadlallah, S.; Leephakphumphanich, W.; Ruscassier, N.; Zoghlami, A.; Allais, F.; Perré, P. Online Microfluidic Production of Sustainable Cyrene™-Derived Porous Microparticles. *Sustainability* **2023**, *15*, 2023. https://doi.org/10.3390/su15032023

Academic Editor: Matthew Jones

Received: 22 December 2022
Revised: 9 January 2023
Accepted: 18 January 2023
Published: 20 January 2023

1. Introduction

Porous microparticles are typically categorized based on their size, size distribution and the presence of predefined pores on their surface and within. They have a broad range of applications as ion exchange resins [1], catalyst supports [2] and tissue regeneration scaffolds [3], to name a few. The porosity of porous microparticles plays a significant role in determining the capacity efficiency of the microparticles and influences the release kinetics [4], where the size and the structure of the pores are the crucial factors affecting the properties of porous microspheres. The same traditional processes used to produce non-porous microparticles may be used to produce porous ones (i.e., atomization [5–7], solvent evaporation [8], suspension polymerization [9]) but with the addition of a pore-forming agent (porogen). The porogen is usually unreactive towards the other materials involved in the process and works according to a solvent casting/particulate leaching mechanism. Although conventional production processes may provide a 90–100% yield, the produced microparticles have a wide size distribution, making them complicated to use in applications that require a highly controlled release (e.g., drug delivery). In addition, they can be energy-consuming, product-consuming and expensive (as in the case of atomization) [10], or they can require expensive post-processing either to solidify (as in coacervation) or to purify from surfactants and polymer adjuvants (as in suspension polymerization) [11].

On the other hand, microfluidics is a simple two-step process in which a droplet—called a chip—is formed in micrometric channels in the first step [12,13]. The droplets are solidified in the second step, either inside the chip before collection (in-situ) or after collection (off-chip). The latter requires a stable formulation in which droplets do not interact or coalesce, while avoiding channel clogging is the greatest challenge governing in situ polymerization [14]. The precise control of droplet formation in microfluidics permits the synthesis of microparticles that are porous or non-porous, as well as simple or core-shell, with a narrow size distribution (coefficient of variation (CV) < 5%) and an almost quantitative yield [15–20]. The potential of microfluidics is also represented in its scalability, where it is possible to implement thousands of millimetric parallel microfluidic devices that can ensure industrial-scale production at a low cost [15]. For example, Busatto et al. [17] prepared lignin microparticles by both traditional solvent evaporation methods and microfluidics combined with off-chip solvent evaporation. Unsurprisingly, the coefficient of variation of microparticle size was four times lower in the microfluidic process (CV = 6.1%) than in the traditional solvent evaporation (CV = 26.5%). Furthermore, simply by tuning the flow rates of the microfluidic system, Nie et al. [21] successfully controlled the size of a double emulsion droplet and the number of encapsulated core spheres by using in situ UV polymerization to form the microparticles. Therefore, precise size control, reproducibility, high yield and scalability make microfluidics a potential candidate for the sustainable production of polymer microparticles of different shapes—including porous microparticles [11].

In this context, Dubinsky et al. [18] synthesized poly(glycidyl methacrylate-*co*-ethylene glycol dimethacrylate) (poly(GMA-co-EGDMA)) porous microparticles via the insitu UV polymerization of the droplets, and the porosity was controlled by changing the nature and concentration of the porogen. Similarly, Zhang et al. [22] applied the same technique to produce poly(hydroxyethyl methacrylate–methyl methacrylate) (poly(HEMA–MMA)) microspheres with two distinct structures (hollow and porous) by employing two different porogens in the process. In another study, Kim et al. [23] prepared drug-loaded poly(lactic-co-glycolic acid) (PLGA) porous microparticles using a phosphate buffer solution porogen by applying microfluidics and off-chip solvent evaporation. The use of porogen is an efficient way to control a particle’s porosity; however, it can encounter several problems: (i) leaching that may remove not only the porogen but also active ingredients and (ii) the long time required to completely leach out the porogen [4]. In a recent study, Xu and Nisisako [19] were able to form more porous microcapsules without the use of porogens by simply changing the polymerization method from off-chip UV to off-chip thermal initiation. This enables the production of porous microparticles and avoids the disadvantages of porogen employment.

Regardless of the outstanding advantages of microfluidic technology in producing controllable porous microparticles, sustainable production using these systems requires consideration of the green aspects of the raw materials as well as the synthesis processes that must avoid or minimize the use of toxic solvents and reagents. In a recent review [11], we extensively discussed the polymeric raw materials used in encapsulation processes and classified them based on their origin into (1) fossil-based, being produced from burning fossil fuels, such as petroleum (e.g., Poly(methyl methacrylate) (PMMA), Polyvinyl chloride (PVC), etc.); (2) naturally occurring bio-based material (e.g., alginate, starch, lignin, etc.); and (3) synthetic bio-based material (e.g., polysaccharides). Microparticles synthesized from fossil-based sources showed better tunability and properties; however, they are non-sustainable by definition due to the regression of petroleum and the greenhouse effect from burning fossil fuels [24]. On the other hand, although naturally occurring raw materials are renewable, they may be complicated to modify and tune. For example, lignin has a very complex structure [25]; alginate is unstable and depolymerizes at 40 °C [26]; and chitosan is mechanically poor and sensitive to storage conditions [27]. Undoubtedly, renewable green raw materials are necessary for sustainable production; however, these problematic factors of naturally occurring polymers leave ample room for improvements that could be based on the exploration of bio-based tunable platform molecules. In this context, levoglucosenone (LGO), an α,β-unsaturated ketone obtained through the catalytic flash pyrolysis of cellulose-based feedstock like bagasse and sawdust, arises as a promising candidate for producing bio-based monomers [28–30]. The potential of LGO is presented by its readily reactive functional moieties that are possible to chemically modify. For instance, the hydrogenation of its conjugated double bond was achieved to produce Cyrene™ (Scheme 1) [31–33] by Circa Group (Tasmania, Australia). Cyrene™ is known to be a green and non-cytotoxic polar aprotic solvent that can be an environmentally friendly substitute for toxic solvents, such as dimethyl formamide (DMF) and acetonitrile. The outstanding performance of Cyrene™ as a solvent has recently been examined in a variety of chemical reactions [34–38], including polymerizations (i.e., enzymatic polycondensation, [39] ring-opening metathesis polymerization (ROMP) [40] and radical polymerization [41]). Saito et al. [41] reported the synthesis of the acrylic derivative of Cyrene™ (m-Cyrene) using a two-step process. The first step involves the reduction of the ketone moiety of Cyrene™ using $LiAlH_4$ in diethyl ether (Et_2O) to obtain levoglucosanol at a 95% yield (Scheme 1). The levoglucosanol (Cyrene-OH) can then be converted into m-Cyrene™ in the presence of methacrylic anhydride (MAN) and 4-dimethylaminopyridine (DMAP) in ethyl acetate for an 85% isolated yield. The free radical (co-)polymerization of m-Cyrene was described by Saito et al. [41] for the preparation of different acrylic bio-based-(co-)polymers based on Cyrene™.

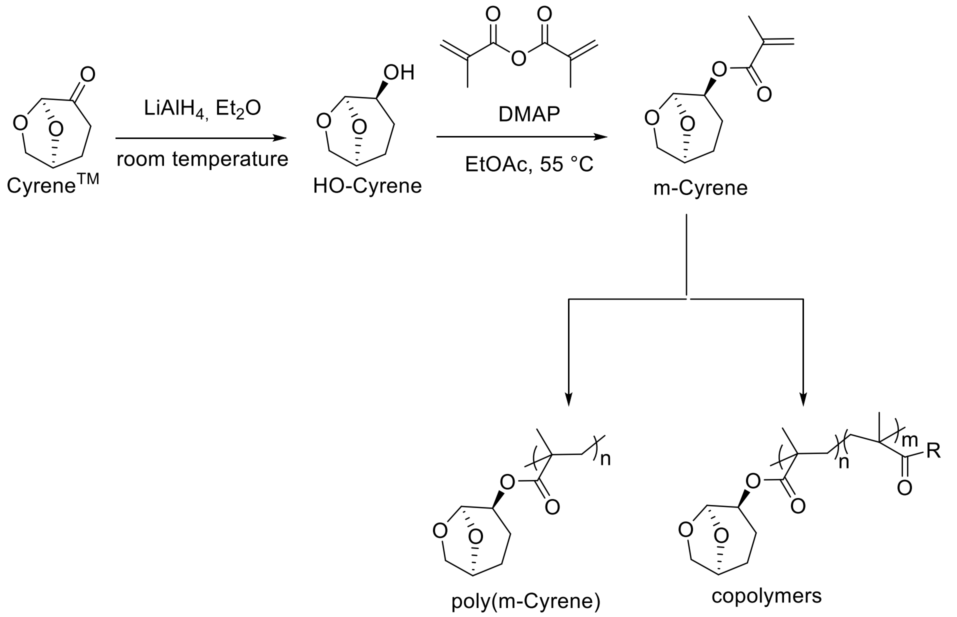

Scheme 1. Synthesis of m-Cyrene and its polymerization to produce Cyrene™-based (co-)polymers. Reproduced from Saito et al. [41] with permission from Royal Society of Chemistry, copyright 2019.

Inspired by the work of Saito et al. [41], we decided to take advantage of both Cyrene™ as a renewable molecule and the microfluidic technique to produce unprecedented bio-based polymer microparticles with controlled porosity. Firstly, m-Cyrene was prepared according to the previously reported procedure [41]. Then a UV-initiated co-flow microfluidic device was developed for the online production of poly (m-Cyrene-co-MAN) microparticles from O/W controlled-size droplets. The effect of the photoinitiator concentration, surfactant concentration and flow rates was studied. Finally, two distinct porosities were obtained without the use of porogens and only by altering the concentration of MAN in the mixture.

2. Materials and Methods

2.1. Chemical Compounds

Dihydrolevoglucosenone (Cyrene™, $C_6H_8O_3$, 128.3 g.mol^{-1}) was received from Circa Group. Sodium borohydride ($NaBH_4$, 37.83 g.mol^{-1}) and lithium aluminum hydride ($LiAlH_4$, 37.95 g.mol^{-1}) were purchased from Sigma-Aldrich, UK, and used as reducing agents. Diethyl ether ($(C_2H_5)_2O$, Et_2O) and methanol (CH_3OH) were purchased from Sigma-Aldrich, UK, and used as solvents. Sodium dodecyl sulfate (SDS, $NaC_{12}H_{25}SO_4$, 288.38 g.mol^{-1}), sodium sulfate decahydrate ($H_{20}Na_2O_{14}S$), 4-dimethylaminopyridine (DMAP, $C_7H_{10}N_2$,122.17 g.mol^{-1}), methacrylic anhydride (MAN, $C_8H_{10}O_3$, 154.16 g.mol^{-1}), saturated sodium bicarbonate solution ($NaHCO_3$), anhydrous magnesium sulfate ($MgSO_4$), 2,2-dimethoxy-2-phenylacetophenone (DMPA) and ammonium persulfate were purchased from Sigma-Aldrich, UK. Citric acid ($C_6H_8O_7$) was purchased from VWR Chemicals. Ethyl acetate ($C_4H_8O_2$) was purchased from Fisher Scientific, UK.

2.2. Monomer Synthesis

The synthesis of m-Cyrene™ was adapted from the work of Saito et al. [41]. Levoglucosanol (Cyrene-OH) was first synthesized from Cyrene™ via the reduction of the ketone moiety. Then the transesterification reaction of Cyrene-OH was performed to obtain methacrylated Cyrene (m-Cyrene).

2.2.1. Synthesis of Levoglucosanol (Cyrene-OH)

Cyrene™ (10.0 g, 78.0 mmol) was dissolved in 125 mL of methanol. The solution was cooled to 0 °C using an ice bath. Then a reduction reaction was performed by slowly adding $NaBH_4$ (4.43 g, 117 mmol) over a period of 20 min. Stirring was continued at 0 °C for 30 min. The ice bath was removed, and the reaction was allowed to stir at room temperature for 12 h. Thereafter, 10 mL of acetone was added, and then 40 mL of citric acid solution (20 wt.%) was added dropwise. The mixture solution was filtered with Celite, and volatiles were removed using a rotary evaporator. The resulting product was dried using a Schlenk line to remove the last traces of solvents and to create a yellow viscous liquid of Cyrene-OH with a 92% yield. ^1H and ^{13}C NMR analysis were in agreement with the chemical shifts reported by Saito et al. [41].

2.2.2. Synthesis of Methacrylated Cyrene (M-Cyrene)

Cyrene-OH (5 g, 38.5 mmol) and DMAP (0.05 g, 0.38 mmol) were charged into a Schlenk round-bottom flask, followed by the addition of 12.5 mL of ethyl acetate. A solution of MAN (5.93 g, 38.5 mmol in 5 mL of ethyl acetate) was added dropwise and stirred for 3 h under a nitrogen atmosphere. Thereafter, the mixture was heated at 50°C and left to stir for 24 h under a nitrogen atmosphere. After the reaction, the solution was diluted with 100 mL of ethyl acetate followed by filtration. Then the liquid portion was extracted via liquid–liquid extraction by using a saturated $NaHCO_3$ solution to separate the liquid into two layers: an aqueous layer and an organic layer. The organic layer was washed three times and then collected and dried with anhydrous $MgSO_4$. The mixture was filtered, and volatiles were removed by using a rotary evaporator. The resulting product was dried using a Schlenk line to remove the last traces of solvents and to create m-Cyrene as a colorless viscous liquid with a 79% yield. ^1H and ^{13}C NMR analyses were in agreement with the chemical shifts reported by Saito et al. [41].

2.3. Droplet Formation and Polymerization in the Microfluidic Device

Two syringe pumps (Harvard Apparatus 11 Pico Plus Elite, Holliston, MA, USA)—one of which was equipped with a 10-mL Hamilton gas-tight glass syringe (P1) and the other with a 500-µL Hamilton gas-tight glass syringe (P2)—were used for the delivery of the continuous phase composed of SDS (a surfactant possible to extract from coconut and palm oils) [42] solution in water, and the dispersed phase (solution of m-Cyrene and MAN with DMPA initiator), respectively, at a controlled flow rate through polytetrafluoroethylene (PTFE) tubing (inner diameter: ID = 0.79 mm, outer diameter: OD = 1.58 mm, length: L = 450 mm) to the microfluidics device (Figure 1). The microfluidics device has a co-flow capillary-based configuration composed of two concentric capillary tubes: an outlet glass capillary tube (T_o) (ID_o = 580 µm, OD_o = 1 mm, L_o = 152 mm, World Precision Instruments Germany GmbH) for the continuous phase and an inlet-fused silica capillary tube (T_i) (ID_i = 100 µm, OD_i = 190 µm, L_i = 75 mm, Postnova Analytics GmbH, Landsberg am Lech, Germany) for the dispersed phase. At the tip of the inlet tube, the dispersed phase (monomer solution) stream was segmented by the continuous phase to form monomer solution droplets that were subsequently delivered through the outer tubing into a 50-mL Erlenmeyer flask containing 10 mL of the continuous phase solution under stirring.

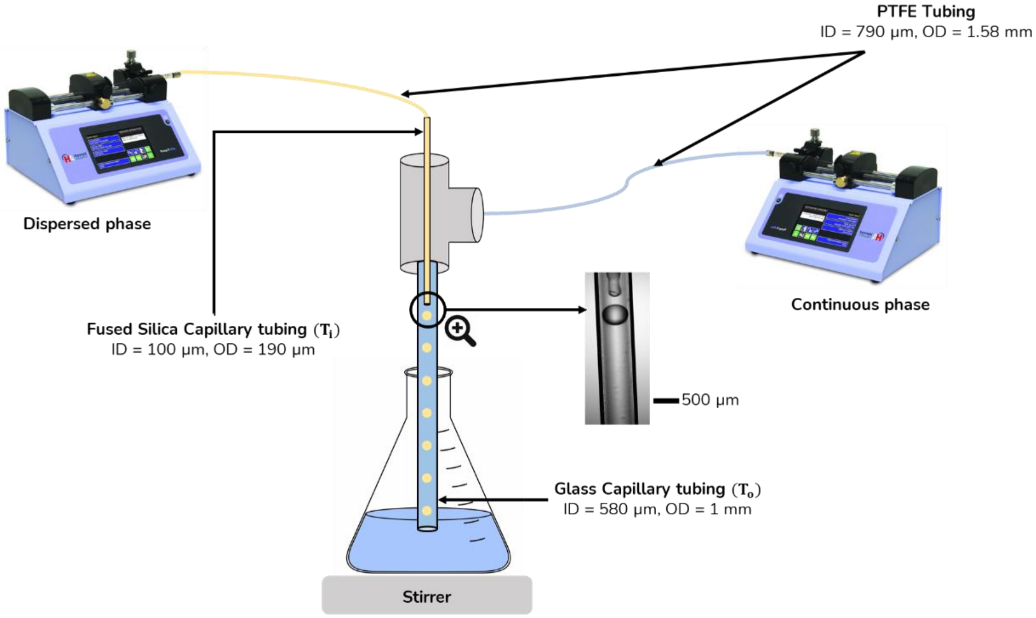

Figure 1. The co-flow microfluidics device.

The system was turned on a t = 0 at constant flow rates to form droplets of controlled size until the 10 mL syringe mounted on P1 became empty. The UV-initiated polymerization was carried out online until t = 1 h using a UV lamp (STERILUV Trio UVA UVB UVC Compact 230 V/P190 W, λ = 265 nm) in two different ways, as shown in Figure 2: (a) in-situ: the system functioned for 1 h, during which the outer capillary tubing was directly exposed to UV-light and droplets were solidified inside it; (b) off-tubing: the system was turned on for 1 h, during which the droplets were exposed to UV-light starting from the moment they exited the glass tubing to the flask until the end of the experiment.

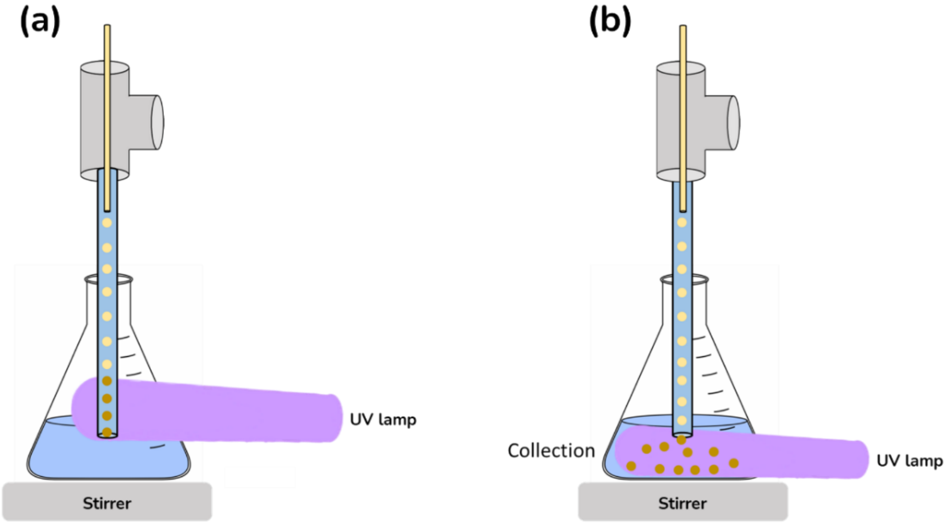

Figure 2. The different polymerization configurations: (**a**) in-situ; (**b**) off-tubing.

2.4. Fluid Characterization and Properties

The fluids used in this study are listed in Table 1 with their corresponding notations, densities and viscosities. The density (ϱ) was measured by injecting 3 mL of the fluid sample using a Thermo F1 micropipette (1–10 mL) and weighing it using a Mettler Toledo XPE105 balance (precision 0.01 mg). The measurements were repeated three times, and the average was calculated. The viscosities of the fluids were measured using a HAAKE MARS iQ Air Rheometer. The variation of the photoinitiator in the co-monomers between 0.25 and 1 wt.% did not have a significant impact on the viscosity. Similarly, the variation of SDS concentration in water between 0.25 and 1 wt.% did not change the viscosity.

Table 1. The physical properties of fluids used in the present study.

Fluid	**Notation**	**Density ϱ (g/mL)**	**Viscosity μ (cP)**
Dispersed phase			
99 wt.% m-Cyrene and 1 wt.% MAN, with 0.25 wt.% DMPA	D1	1.07 ± 0.007	4.2 ± 0.04
99 wt.% m-Cyrene and 1 wt.% MAN, with 0.5 wt.% DMPA	D2	1.07 ± 0.007	4.2 ± 0.04
99 wt.% m-Cyrene and 1 wt.% MAN, with 1 wt.% DMPA	D3	1.07 ± 0.007	4.2 ± 0.04
8 wt.% m-Cyrene and 92 wt.% MAN, with 0.25 wt.% DMPA	D4	1.02 ± 0.006	18 ± 0.18
8 wt.% m-Cyrene and 92 wt.% MAN, with 0.5 wt.% DMPA	D5	1.02 ± 0.006	18 ± 0.18
8 wt.% m-Cyrene and 92 wt.% MAN, with 1 wt.% DMPA	D6	1.02 ± 0.006	18 ± 0.18
Continuous phase			
1.25 wt.% SDS in water	A1	1 ± 0.002	1.5 ± 0.01

The interfacial tension (γ) between the dispersed and aqueous continuous phases was measured by a GBX Digidrop DGD-MCATV6 tensiometer using the pendant droplet method (reported in Table 2). To measure the γ between the two continuous phase liquids (A1 and A2) and the dispersed phase solutions (D4–D6), a 1-μL pendant droplet of the latter was formed in an optical cell containing the continuous phase. The surface tension was then measured, and the droplet formation and interfacial tension measurement were repeated two more times to calculate an average. Since the critical micellar concentration (CMC) of SDS was 8.2 mM (equivalent to 0.2 wt.%), all the surfactant solutions of this study were above the CMC. This explains the non-variation of γ with the concentration of SDS in the continuous phase. The interfacial tensions between solutions (D1–D3) and A1 and A2 were too small to form a pendant droplet and be measured.

Table 2. The surface tensions between dispersed and continuous phases.

Dispersed \ Continuous	γ (mN/m)
	A1
D1	Very small to be measured using a GBX tensiometer
D2	
D3	
D4	1.8 ± 0.3
D5	
D6	

2.5. Imaging

The droplet formation images were acquired using a Zeiss Axio Zoom.V16 stereo microscope (Carl Zeiss Microscopy GmbH, Germany) equipped with a charged-coupled device (CCD) camera (Hamamatsu ORCA-flash4.0LT, 30 fps maximum framerate) and controlled using Zeiss Zen 2.6 (blue edition, ZEISS, Germany) software, using the objective Apo Z 1.5×. The image resolution was 2048 × 2048 pixels, which represents a field width of 4.16 mm × 4.16 mm.

The size, shape and morphology of the formed polymer microparticles were observed using an environmental scanning electron microscope (ESEM, FEI Quanta 200) in low vacuum mode. Samples were mounted on an aluminum stub using double-sided carbon tape. The diameters of the droplets and microparticles were determined as the average of 10–30 microparticles measured using ImageJ 1.53t software. The CV of the microparticles was calculated as the ratio between the relative standard deviation of their diameters and the average diameter.

The 3D microstructures of microparticles were acquired via X-ray tomography (EasyTOM XL 150/160, RX-solution, France). The tomography configuration was set up with a nano-source (LB6 filament), a CCD camera of 2016 × 1344 pixels, a pixel size of 0.4 μm, an exposure time of 1 s per frame and an average of 10 frames per projection. The X-ray source voltage was set at 100 kV, and the working current was 190 μA. For these acquisition parameters, each scan lasted approximately 4 h, and approximately 1440 projections were recorded. The reconstruction was performed using X-Act software 22.06 (RX-Solutions, France) to produce 3D images, which were further analyzed in Avizo 2019.2 (Thermo Fisher Scientific, Waltham, MA, USA).

First, 3D volume visualization of the stacks was performed by applying the Volume Rendering tool. Second, subvolumes were extracted from the original datasets and processed using a 3D "median filter" to reduce the noise. Next, the background was removed using the "watershed" tool from the segmentation editor. Then thresholding was applied to separate the pores from the matrix. Thereafter, the 3D volume of the matrix and the pores were obtained using the "materiel statistics" function. The pore volume fraction was calculated by dividing the 3D volume of the pores by the total 3D volume. Finally, the "labeling" tool was applied to assign pores as individual particles, thereby facilitating the quantification of their 3D volumes by using the "label analysis" function.

3. Results

The in-situ and off-tubing online polymerization of m-Cyrene monomer droplets without MAN did not yield microparticles with photoinitiator concentrations at 1 and 5 wt.%. Instead, polymeric aggregates were formed (see Supplementary Information). On the other hand, the microparticles blocked the tubing and caused clogging in certain in-situ polymerization experiments of m-Cyrene-MAN droplets (92 wt.% of MAN) at sizes ≈ 500 μm—close to that of the capillary tubing's inner diameter (ID = 580 μm). As a result, the next microparticles were blocked behind the previous ones, forming a tail shape (see Figure 3). The clogging of the tubing made the continuous production process nonfeasible;

however, this implies that the polymerization time is estimated to be less than the residence time (<10 s).

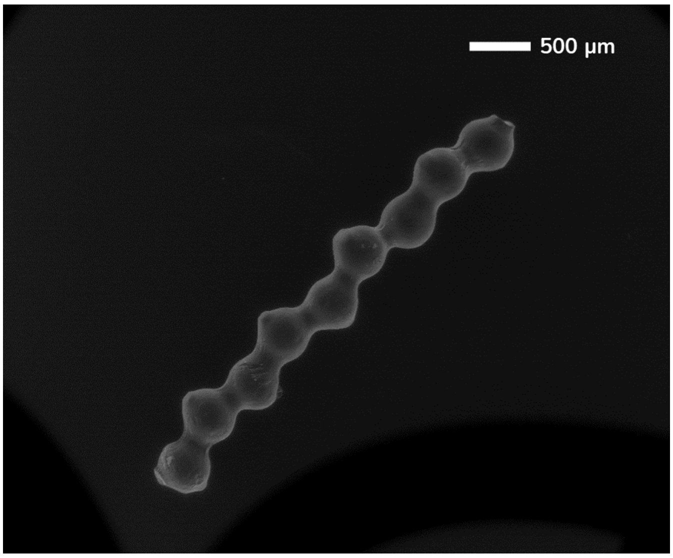

Figure 3. ESEM image of the microparticles arranged in a string-like shape after in-situ polymerization. Experimental parameters: mixture R1, Q_c = 10 mL/h; Q_d = 0.1 mL/h; C_P = 1 wt.%; C_s = 1.25 wt.%.

Therefore, we studied the online formation of polymer microparticles from a monomer mixture of m-Cyrene and MAN. We adopted off-tubing polymerization to avoid clogging problems and to have a continuous performing system, regardless of the droplet size. After polymerization, the formed microparticles were suspended in the SDS solution in the flask at the end of the experiment. The suspension was then centrifuged at 3000 rpm for 10 min using a Beckmann Coulter Allegra X-15R and rinsed three times with deionized water to remove excess SDS. The continuous phase was removed by decantation, and the microparticles were dried under a vacuum overnight to remove any remaining traces of water.

The shape and porosity of the produced polymer microparticles are influenced by parameters like the photoinitiator and surfactant, their respective concentrations and the flow rates. The concentration of the photoinitiator in the dispersed phase and that of surfactants in the continuous phase should be sufficient for this process. However, it is also worthwhile to employ fewer raw materials in the process from a sustainability perspective and to facilitate the purification post-processing—especially in the case of up-scaling. Therefore, we discuss the impact of reducing the photoinitiator concentration on the formed polymer microparticles for two different monomer mixtures: R1 with MAN at 1 wt.% and R2 with MAN at 92 wt.%. The influence of flow rates Q_c and Q_d on droplet formation and microparticle synthesis is then discussed in both compositions. The latter affects the microparticle porosity, which was analyzed by microtomography.

3.1. Effect of Photoinitiator Concentration

As mentioned in the study of Kiatkamjornwong et al. [43], photoinitiator concentration (C_P) affects the polymerization reaction and microparticle shape. In this section, we investigate the influence of C_P on the polymerization of two different monomer mixture droplets: R1 (1 wt.% MAN, 99% m-Cyrene) and R2 (92 wt.% MAN, 8 wt.% m-Cyrene). The droplets were formed using both mixtures (R1 and R2) with three distinct photoinitiator concentrations (C_P = 0.25, 0.5 and 1 wt.%), while the continuous phase was 1.25 wt.% SDS solution in water (C1 in Table 1) and flow rates were fixed at Q_c = 10 mL/h and Q_d = 0.1 mL/h in all experiments presented in Table 3. Due to its surface tension, which was too small to be measured, the monomer mixture R1 experienced a substantial translation over a short time scale while exiting the capillary tube, leading to the formation of a narrow thread between the droplet and the capillary tube. The thread then broke into droplets with an average size of 250 μm and a CV of 3.7%, at a frequency of approximately 1 drop/s in experiments E1–E3 (Figure 4a). On the other hand, the droplets formed from R2 had a higher surface tension (experiments E4–E6) and followed a periodic dripping regime (see Figure 4b). Contrary to the case of R1, the surface tension of R2 was stronger and sufficient to hold the droplet to the capillary tube for a longer time; thus, droplets had a larger volume before detaching. As a result, the size of droplets formed by R2 ($\bar{d}$ ≈ 500 μm, CV = 2%) was double that of the droplets formed by R1, with a lower droplet formation frequency (approximately 0.4 drop/s).

Table 3. Parameters of experiments conducted to study the effects of photoinitiator concentration.

Exp.	Monomer Mixture	Dispersed Phase	Continuous Phase	Q_c (mL/h)	Q_d (mL/h)	C_P (wt.%)	C_s (wt.%)	$\bar{d}$ (μm)
E1	R1	D1	A1	10	0.1	0.25	1.25	250
E2	R1	D2	A1	10	0.1	0.5	1.25	250
E3	R1	D3	A1	10	0.1	1	1.25	250
E4	R2	D4	A1	10	0.1	0.25	1.25	500
E5	R2	D5	A1	10	0.1	0.5	1.25	500
E6	R2	D6	A1	10	0.1	1	1.25	500

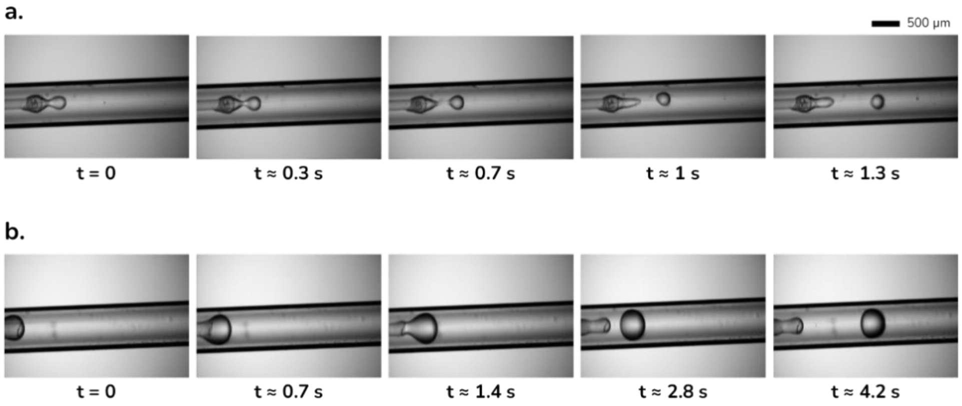

Figure 4. Droplet formation stages for different dispersed phases. (**a**) R1: Q_c = 10 mL/h, Q_d = 0.1 mL/h, C_s = 1.25 wt.% and C_P = 1 wt.%; (**b**) R2: Q_c = 10 mL/h, Q_d = 0.1 mL/h, C_s = 1.25 wt.% and C_P = 1 wt.%.

The system was turned on for 1 h in all experiments, while polymerization occurred in the vials as previously described. At the end of the experiment, the collected microparticles were observed using an ESEM. Figure 5 presents the ESEM images for experiments using monomer mixture R1 (1 wt.% MAN, 99 wt.% m-Cyrene: E1, E2 and E3 in Table 3) after polymerization. At C_P = 0.25 wt.% (E1), a solid powder was obtained. However, ESEM images indicate that the microparticles did not have a spherical shape (Figure 5A). This is likely because the droplets experienced coalescence and/or deformation before solidification. At C_P = 0.5 wt.% (E2), the microparticles formed aggregates with microspheres on the surface that were distorted (Figure 5B). Both situations could be avoided by collecting the O/W emulsion and ensuring its temporal stability of droplet shape and interface before polymerizing. However, this would require a deeper study of the colloidal system, which is beyond the goal of the present paper (i.e., the rapid online production of polymer microparticles). At C_P = 1 wt.% (E3), we obtained a white powder in the collection flask, which appeared to be composed of spherical microparticles with a narrow size distribution ($\overline{d_m}$ = 160 μm, CV = 5%, average aspect ratio χ = 1.05) based on the ESEM microscopy images (Figure 5C). This suggests that the higher concentrations of photoinitiator accelerated the UV polymerization process. Indeed, at C_P < 1 wt.%, the droplets remained in a liquid state in the Erlenmeyer flask, where they experienced coalescence and deformation under stirring before the completion of UV polymerization. On the other hand, with a concentration C_P of 1%, the polymerization reaction was completed at the moment of collection, where microparticles with a homogeneous size were obtained. Similarly, non-spherical particles were obtained from co-monomer R2 with 92 wt.% MAN and 8 wt.% m-Cyrene at C_P = 0.25 wt.% (Figure 6A), and aggregates of microparticles varying in size were presented at C_P = 0.5 wt.% (Figure 6B). However, a concentration C_P of 1% yielded polymer microparticles in the form of beads with $\overline{d_m}$ = 330 μm, CV = 2.5% and χ = 1.15 (Figure 6C). These results show the sensitivity of the process to a photoinitiator concentration of 1 wt.%, which is the minimum required for the online production of microparticles from mixtures R1 and R2. This concentration was used for all experiments in the following parts.

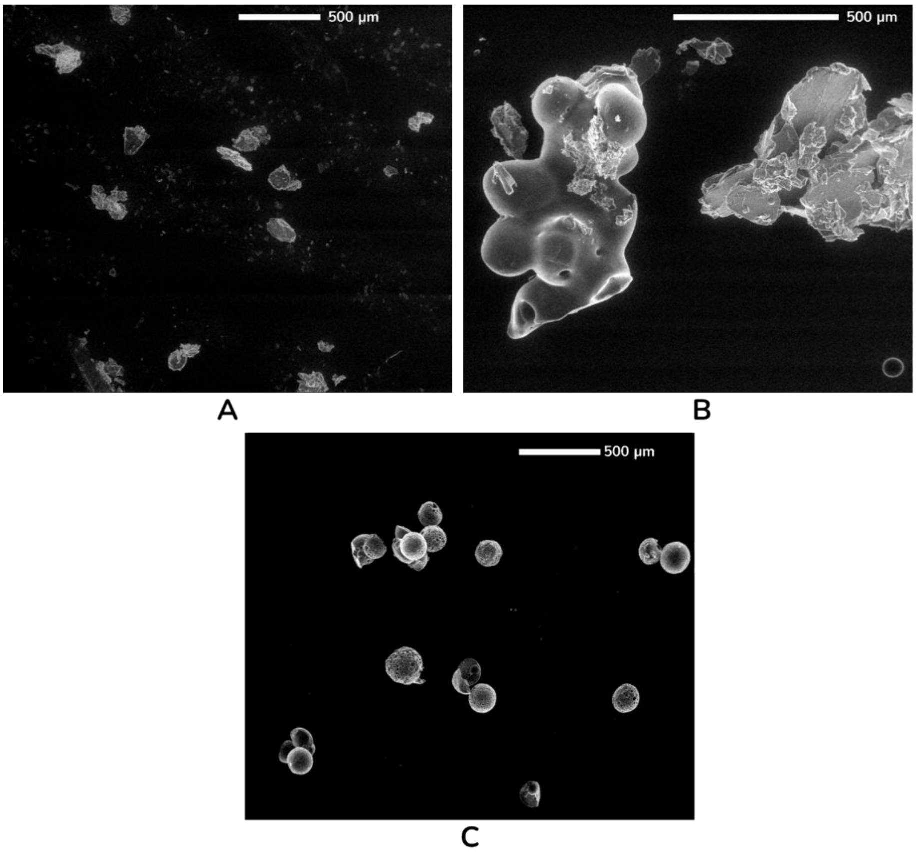

Figure 5. SEM images of experiments: (**A**) E1 with C_P = 0.25 wt.%; (**B**) E2 with C_P = 0.5 wt.%; (**C**) E3 with C_P = 1 wt.%. The co-monomer is R1, and the experimental parameters are reported in Table 3.

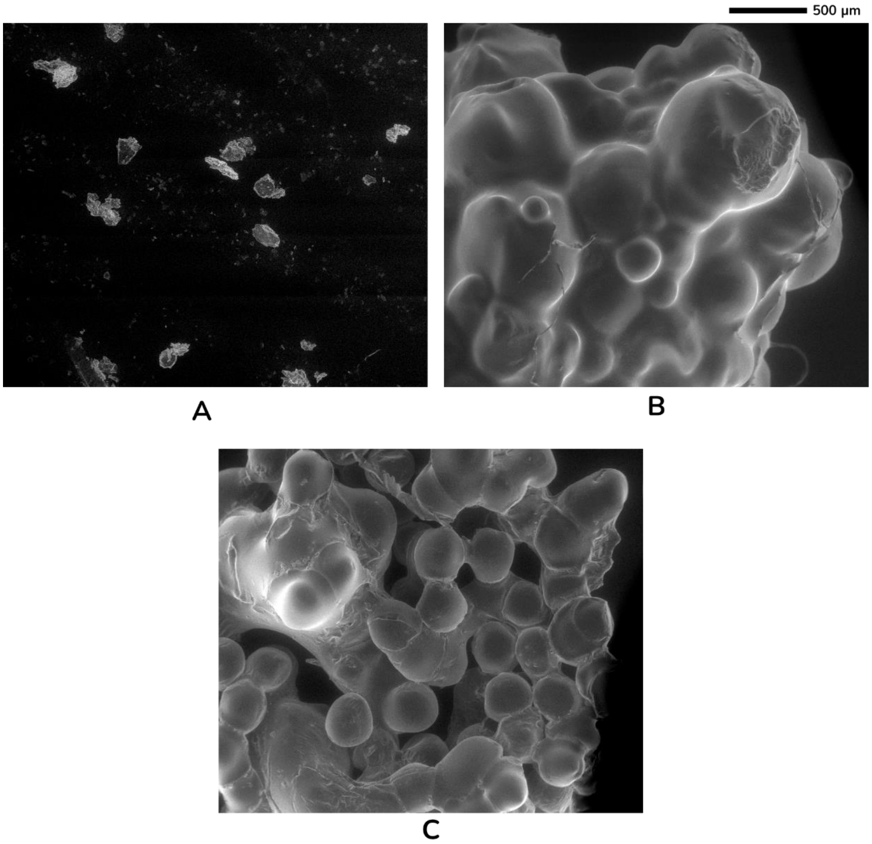

Figure 6. ESEM images of experiments: (**A**) E4 with C_P = 0.25 wt.%; (**B**) E5 with C_P = 0.5 wt.%; (**C**) E6 with C_P = 1 wt.%. The co-monomer is R2, and the experimental parameters are reported in Table 3.

3.2. *Effect of Flow Rate*

The concentration of the photoinitiator was fixed at C_P = 1 wt.%, based on the previous results, and the concentration of SDS surfactant in the continuous phase was fixed at C_s = 1.25 wt.%, which corresponds to five times the CMC required to cover the droplet interface. The flow rate of the dispersed phase Q_d varied between 0.1 and 1 mL/h, whereas the flow rate of the continuous phase Q_c varied between 10 and 100 mL/h. Figure 7 presents images of the R1 droplets rising in the continuous phase (A1) at different flow rates, while Figure 8 presents the same information for R2 droplets. The two monomer mixtures show distinct behaviors when segmented by the same continuous phase (A1). R2 was in a dripping regime at all flow rates of the continuous phase for Q_d = 0.1 mL/h; however, for $Q_d \geq 0.2$ mL/h, the dispersed phase underwent a substantial translation over a short time scale while exiting the capillary tube, leading to the formation of a narrow thread between the droplet and the capillary tube. The thread broke and formed droplets with satellite droplets behind them (see Figure 8). On the other hand, due to its low interfacial tension with A1, a jetting regime was instead observed in microscopy images for the experiments of monomer R1, except for E7 (Figure 7). Moreover, the jet length increased with Q_d in accordance with Meister and Scheele's study [44] and then broke up downstream into non-homogeneous-sized droplets by Rayleigh instability as in experiments E8 and E9, where the CV of the droplets were 12 and 32%, respectively. In experiments E10–E15, the liquid jet extended along the entire observation window without recording breakage into droplets. Therefore, the formation of droplets was observed only at Q_d = 0.1 mL/h for R1. Consequently, we fixed Q_d at 0.1 mL/h in the next part to monitor and compare the behavior of both co-monomer droplets after UV-initiated polymerization, as well as to investigate the effect of Q_c.

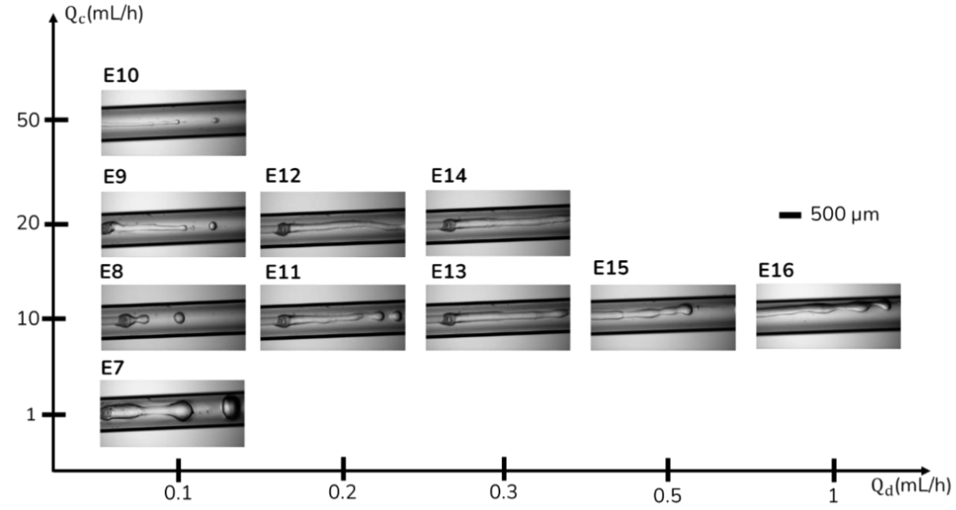

Figure 7. Images of the segmentation of the dispersed phase D3 (co-monomer R1) at different flow rates Q_c and Q_d. C_s = 1.25 wt.% and C_p = 1 wt.%.

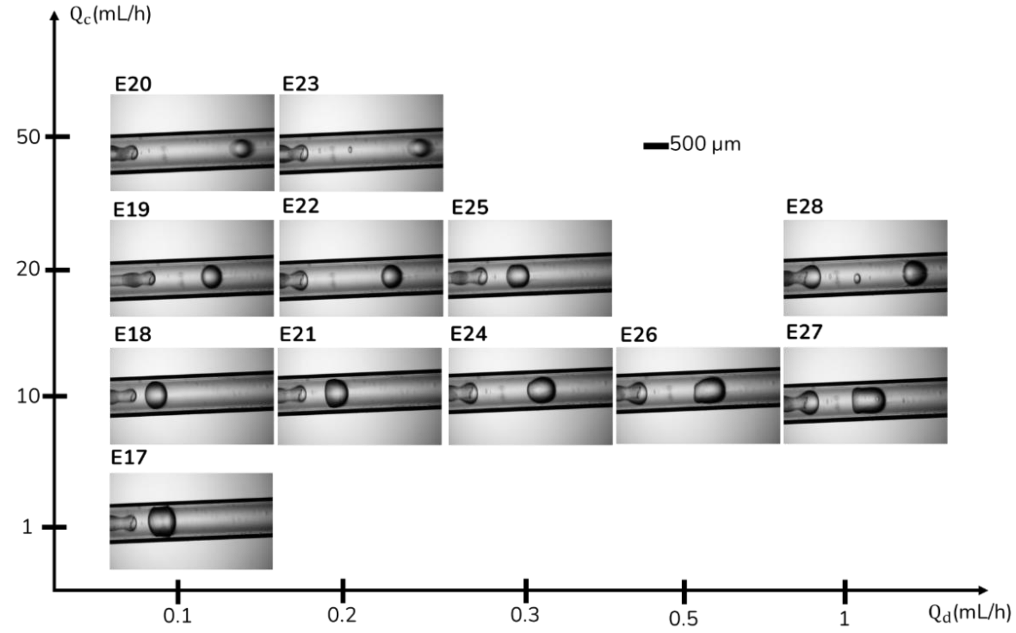

Figure 8. Images of the segmentation of the dispersed phase D6 (co-monomer R2) at different flow rates Q_c and Q_d. C_s = 1.25 wt.% and C_p = 1 wt.%.

The system was turned with both dispersed phases (R1 and R2) at Q_d = 0.1 mL/h (as previously mentioned) and at four values of Q_c: 1, 10, 20 and 50 mL/h, corresponding to Q_c/Q_d = 10, 100, 200 and 500, respectively. Figure 9 presents the variation of the droplet diameter as a function of Q_c/Q_d for R1 and R2. In accordance with the literature results, the droplet size decreased with Q_c/Q_d in both cases due to the higher shearing force exerted on the dispersed phase [45]. However, in the case of R1, experiments E9 and E10 (Q_c/Q_d = 20 and 50, respectively) showed larger error bars in Figure 10 when compared to the error bars of experiments with R2. This is the result of the jet breakup into non-monodisperse droplets in the aforementioned experiments. Table 4 presents the experimental parameters and droplet sizes of all experiments, and Table 5 presents the sizes of droplets and microparticles in experiments using R1 or R2 as the dispersed phase with comparable flow rates. Concerning the experiments with R1, the thread formed in E7 (Q_c/Q_d = 10) was broken into relatively monodisperse droplets (CV = 5.7%; see Figure 7); however, the formed microparticles accumulated together, and it was difficult to distinguish each one of them separately under the ESEM (Figure 10A). As a result, it was not possible to determine the mean size of the polymer microparticles in this experiment. The increase of Q_c/Q_d to 100 (E8) permitted the reduction of monodisperse droplet sizes by approximately a factor of 2 ($\bar{d}$ ≈ 255 μm), while the polymerization yielded a powder composed of spherical microparticles with $\overline{d_p}$ ≈ 160 μm and CV_P = 5% (Figure 10B). Similarly, a powder was obtained at Q_c/Q_d = 200 (E9); however, the microparticles were not monodisperse (CV_P = 17%; see Figure 10C). This dispersion was initiated as the jet broke up into droplets with a wide size distribution. On the other hand, R2 was segmented into monodisperse droplets (CV ≤ 2%) in a dripping mode for all flow rate ratios reported in Table 5, with the droplet size decreasing with the flow rate ratio. Indeed, the droplets in E17 (Q_c/Q_d = 10) had the same size as the inlet diameter of the capillary tube *(*$\bar{d}$ ≈ 580 μm), and monodisperse microbeads were also formed after polymerization, where $\overline{d_p}$ ≈ 416 μm and CV_P = 4% (Figure 11A). The formation of smaller monodisperse droplets at Q_c/Q_d = 100 ($\bar{d}$ ≈ 503 μm and CV = 2%) unsurprisingly led to smaller monodisperse microparticles (where $\overline{d_p}$ ≈ 329 μm and CV_P = 2.6%) in experiment E18 (see Figure 11B). However, at Q_c/Q_d = 200, an aggregate was observed with some spherical microparticles sticking to its surface (see Figure 11C).

Table 4. Parameter of the experiments conducted to study the variation in flow rates. In E9 and E10, droplets were produced by jet breakup. C_P = 1 wt.% and C_s = 1.25 wt.%.

	Monomer Mixture	**Dispersed Phase**	**Continuous Phase**	**Q_c (mL/h)**	**Q_d (mL/h)**	**$\bar{d}$ (μm)**	**CV (%)**
E7	R1	D3	A1	1	0.1	493	5.7
E8	R1	D3	A1	10	0.1	255	3.6
E9	R1	D3	A1	20	0.1	166	12
E10	R1	D3	A1	50	0.1	125	32
E11	R1	D3	A1	10	0.2	-	-
E12	R1	D3	A1	20	0.2	-	-
E13	R1	D3	A1	10	0.3	-	-
E14	R1	D3	A1	20	0.3	-	-
E15	R1	D3	A1	10	0.5	-	-
E16	R1	D3	A1	10	1	-	-
E17	R2	D3	A1	1	0.1	580	1.6
E18	R2	D6	A1	10	0.1	503	2
E19	R2	D6	A1	20	0.1	450	1
E20	R2	D6	A1	50	0.1	340	2
E21	R2	D6	A1	10	0.2	527	2
E22	R2	D6	A1	20	0.2	453	1.7
E23	R2	D6	A1	50	0.2	363	3
E24	R2	D6	A1	10	0.3	545	2.8
E25	R2	D6	A1	20	0.3	478	2.6
E26	R2	D6	A1	10	0.5	566	4.3
E27	R2	D6	A1	10	1	641	6.8
E28	R2	D6	A1	20	1	512	1.4

Table 5. Droplet sizes and their corresponding microparticle sizes, with their corresponding coefficient of variation.

	Co-Monomer	**Q_c/Q_d**	**$\bar{d}$ (μm)**	**CV (%)**	**$\overline{d_p}$ (μm)**	**CV_P (%)**
E7	R1	10	493	5.7	-	-
E8	R1	100	255	3.6	160	5
E9	R1	200	166	12	128	17
E17	R2	10	580	1.6	516	4
E18	R2	100	503	2	329	2.6
E19	R2	200	450	1	-	-

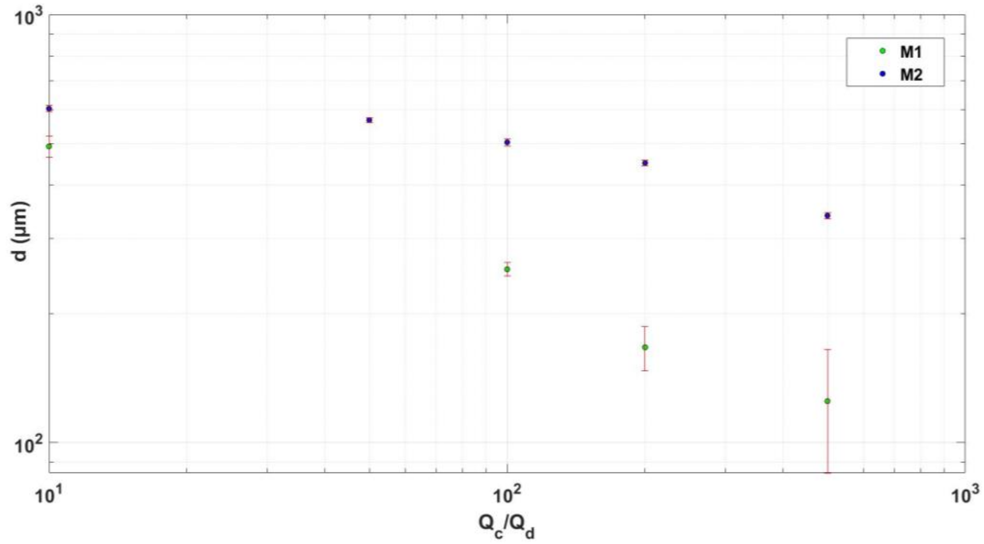

Figure 9. Droplet size variation as a function of Q_c/Q_d for co-monomers R1 and R2 with Q_d = 0.1 mL/h, C_s = 1.25 wt.% and C_p = 1 wt.%. Error bars represent the standard deviation.

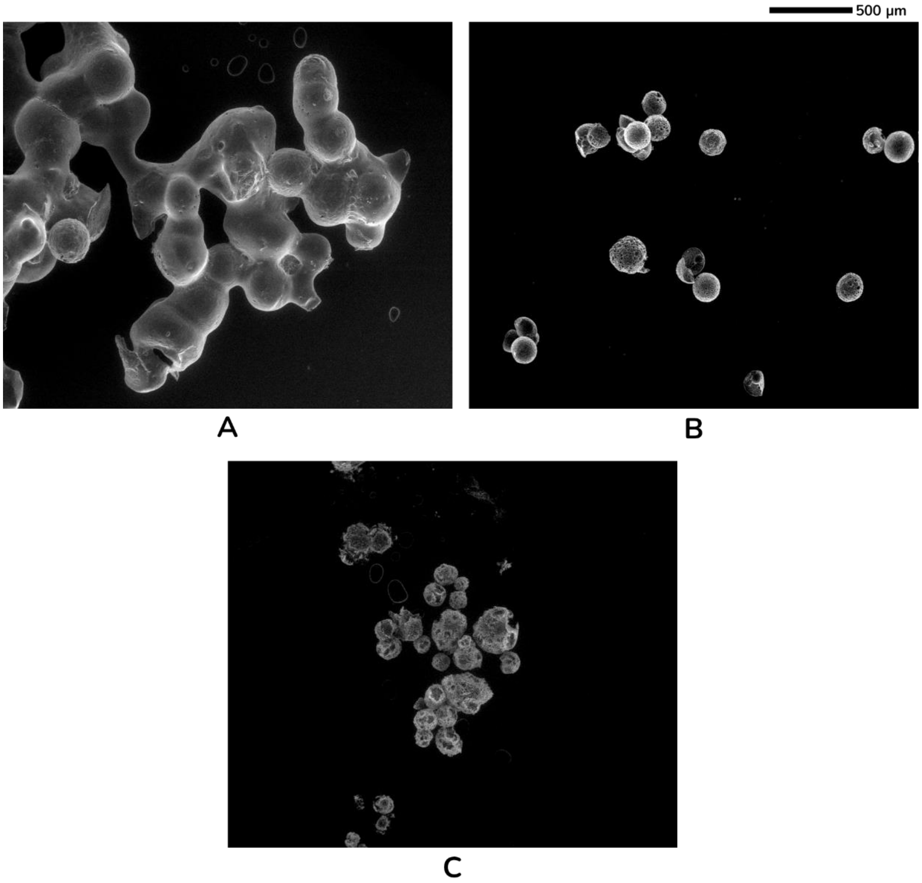

Figure 10. ESEM images after the UV polymerization of R1 droplets for experiments: (**A**) E7: Q_c/Q_d = 10; (**B**) E8: Q_c/Q_d = 100; (**C**) E9: Q_c/Q_d = 200. Q_d = 0.1 mL/h, C_s = 1.25 wt.% and C_p = 1 wt.%.

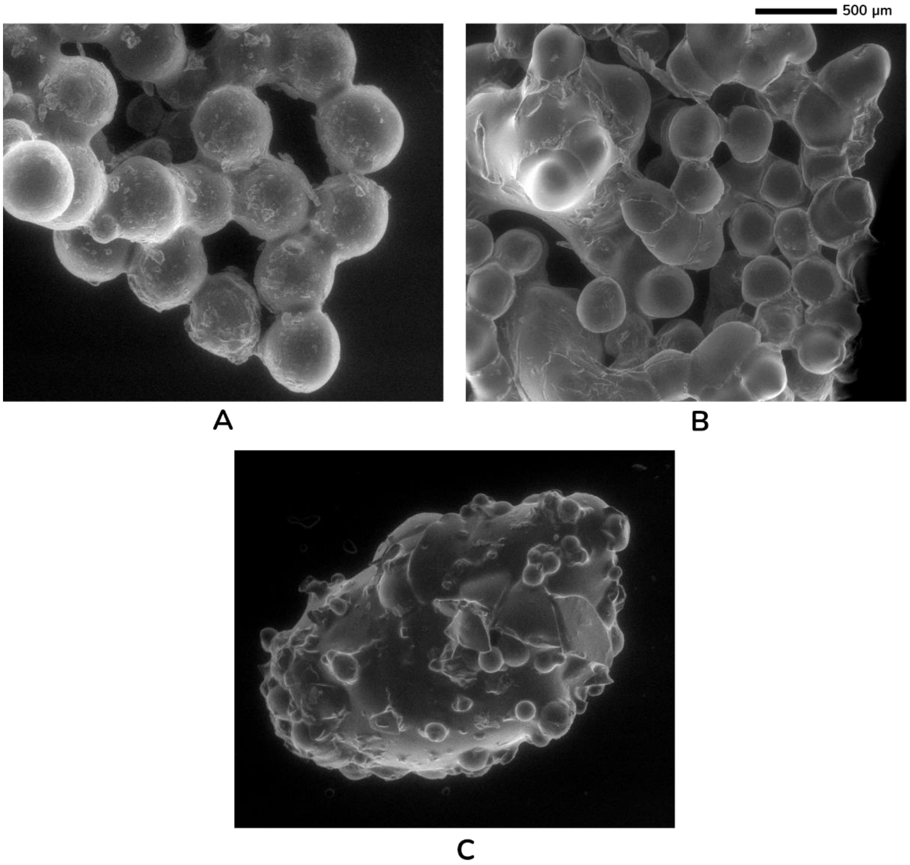

Figure 11. ESEM images after the UV polymerization of R2 droplets for experiments: (**A**) E17: $Q_c/Q_d = 10$; (**B**) E18: $Q_c/Q_d = 100$; (**C**) E19: $Q_c/Q_d = 200$. $Q_d = 0.1$ mL/h, $C_s = 1.25$ wt.% and $C_p = 1$ wt.%.

3.3. Morphology and Porosity

As noted in the previous section, monodisperse microparticles were formed from R1 at $Q_c/Q_d = 100$ (E8) and from R2 at both $Q_c/Q_d = 10$ and 100 (E17 and E18, respectively). In this section, we focus on experiments E8 and E18, which were conducted using the monomer mixtures R1 and R2, respectively, and had the same flow rate ratio Q_c/Q_d, same surfactant concentration and photoinitiator concentration to compare the effects of MAN concentration on the morphology and surfaces of the microparticles. Figure 12A,C presents the SEM images of experiments E8 and E18, respectively. The ESEM images of both microparticles show smooth surfaces despite the different concentrations of MAN used. However, the microparticle of E8 (Figure 12A) seems to be more porous than that of E18 (Figure 12C). Since SEM images give only a qualitative description of the surface and morphology of microparticles, a more advanced and precise technique is required to make a quantitative description of microparticle porosity. Therefore, the same microparticles presented in Figure 12A,C (experiment E8 and E18, respectively) were scanned using X-ray tomography, and the 3D images were reconstructed according to the methodology reported in Section 2.5. The 3D reconstructed images of the microparticles in experiment E8 (Figure 12B) and experiment E18 (Figure 12D) were successful, with a very good resolution (down to 0.4 μm) for one microparticle of d ≈ 160 μm in E8 and 330 μm in E18.

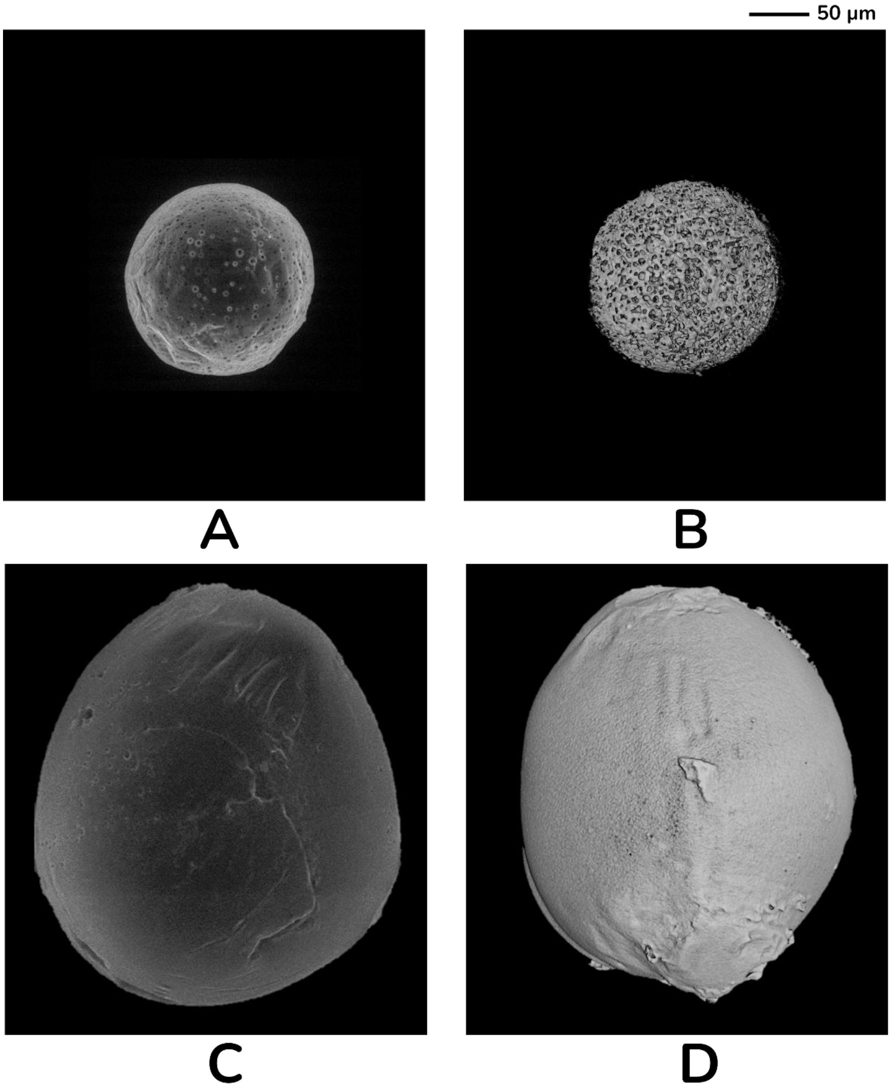

Figure 12. (**A**) ESEM image of a microparticle formed from R1 (E8) and (**B**) the corresponding reconstructed 3D tomographic scan image of the same microparticle. (**C**) The ESEM image of a microparticle formed from R2 (E18) and (**D**) the corresponding reconstructed 3D tomographic scan image of the same microparticle. $Q_c/Q_d = 100$. $Q_d = 0.1$ mL/h, $C_s = 1.25$ wt.% and $C_p = 1$ wt.%.

3D-reconstructed images of the matrices and pores inside the microparticles in experiment E8 (R1) are shown in Figure 13A,C, respectively, while Figure 13B,D represent the same information for experiment E18 (R2). We observed that the 3D images of the matrix in experiment E8 depict more porosity when compared to those for E18. While an ESEM can only show the surface pattern, 3D tomography reveals the pores inside the structure and allows the calculation of the porosity of both microparticles according to the method reported in Section 2.5. In fact, the pores inside the microparticle of experiment E8 ranged between 0.4 and 10 μm, corresponding to 0.24–6% of the microparticle diameter, with 85% of the pores ranging between 1 and 3 μm (0.24–1.8% of the microparticle diameter), and a porosity of approximately 30%. On the other hand, the porosity in E18 was drastically smaller than that of E8 (approximately 2%), with 97% of the pores ranging between 0.4 and 3 μm (0.1–1% of microparticle diameter). This result demonstrates the importance of MAN in the monomer mixture to control the porosity of microparticles, with pores having a relatively homogeneous size in experiments E8 and E18 with drastically different MAN concentrations (1 and 92 wt.%, respectively). MAN concentration seems to be critical for controlling microparticle porosity since 1 wt.% MAN resulted in a microparticle porosity of approximately 30%, while the porosity was only 2% with the 92 wt.% MAN ratio used in E18.

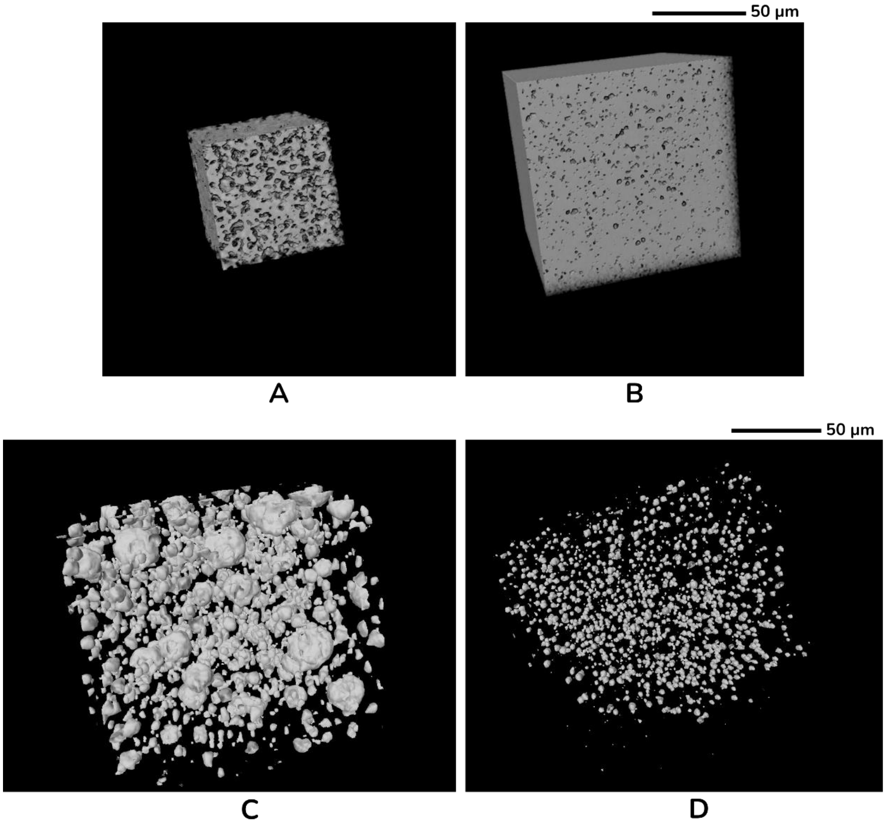

Figure 13. 3D tomographic images of the microparticle matrices of (**A**) experiment E8 (formed from R1) and (**B**) experiment E18 (formed from R2), and the 3D tomographic image of the pores inside the microparticles in experiments (**C**) E8 and (**D**) E18. All presented 3D images were reconstructed from the scans using the nanotomographic source. $Q_c/Q_d = 100$. $Q_d = 0.1$ mL/h, $C_s = 1.25$ wt.% and $C_p = 1$ wt.%.

4. Discussion

In the case of m-Cyrene, the microfluidic online production of polymer microparticles was not possible without the addition of a co-monomer such as MAN, even with a C_p of 5 wt.%. However, the addition of MAN in two different concentrations (1 and 92 wt.%) allowed this production with 1 wt.% of photoinitiator. The reported results have three advantages. From an efficiency perspective, the polymerization reaction was first accelerated. Second, from a sustainability perspective, the reduction of raw photoinitiator material from 5 wt.% down to 1 wt.% decreases the amount of waste generated. Finally, the presence of MAN in the preparation procedure of m-Cyrene avoids excessive and energy-consuming purification processes.

The microfluidic process is known to be rapid, inexpensive and controlled. In this article, we validate the previously reported capability of microfluidics to control the size of microparticles by tuning the flow rate [15,16,19] in the case of monomer R2 (E17 and E18; see Figure 11). The case of R1 showed more limitations since a further increase in Q_d to more than 0.1 mL/h resulted in a jet of the dispersed phase that broke into polydisperse and non-spherical droplets (Figure 7). The experiment with $Q_c = 10$ mL/h and $Q_d = 0.1$ mL/h (E8 and E18) represents an interesting comparison case for both R1 and R2. The variation of the MAN concentration in the dispersed phase from 1 wt.% in R1 to 92 wt.% in R2 drastically changed the viscosity and density of the fluid, and thus the size of the formed droplet. Therefore, the concentration of MAN can serve the same role as flow rates in tuning the droplet size. Moreover, porosity is a significant parameter that determines the capacity efficiency and release kinetics of the encapsulated phase [4]. Thus, controlling the porosity is of particular importance. The 1 wt.% MAN concentration (R1) yielded microparticles with porosity 15 times higher than the 92 wt.% MAN mixture. This results in a total of five advantages of the addition of MAN: (1) accelerating the polymerization reaction; (2) lowering the consumption of raw materials; (3) avoiding excessive purification processes; (4) controlling the droplet size; (5) controlling the microparticle porosity to adapt it to the targeted application. The latter advantage is significant because the ultimate goal is to encapsulate an active ingredient within a micro-polymeric shell constituted of m-Cyrene and MAN, while the control of porosity is equivalent to the control of microcapsule capacity and release kinetics. This is why it was of critical importance to study the behavior of m-Cyrene and MAN mixtures of different ratios when segmented into droplets and polymerized in a microfluidic device before discussing the microencapsulation in this article. The present results introduce the mixture of m-Cyrene and MAN as a potential shell material with a porosity that can be controlled by the concentration of MAN.

5. Conclusions

Cyrene™ is a green bio-based solvent extracted from cellulosic biomass. However, its high cost is considered the main drawback, which limits its use on an industrial scale [46]. The Resolute project, with 11 European partners and a total budget of EUR 23 M, aims to convert waste cellulosic biomass into safe, environmentally friendly chemicals like Cyrene™ on an industrial scale. This will significantly increase production, reduce the price and allow the efficient industrial implementation of green substitutes like Cyrene™. Previous publications have shown that Cyrene™ can be converted into a renewable bio-sourced monomer such as m-Cyrene™ [41]. In this work, we applied the same procedure reported in the literature and took advantage of the produced m-Cyrene™ to form monodisperse droplets and to polymerize them in a microfluidic device. We reported a sustainable and environmentally friendly droplet-based microfluidic process to fabricate the porous microparticles derived from Cyrene™. MAN was used as a co-monomer to accelerate the polymerization of droplets. In addition, the MAN concentration in the mixture was shown to play a similar role to the flow rate in determining the droplet size, with another potential role being to fix the porosity of the microparticle. This original result introduces the possibility of encapsulating an active ingredient with the capability of controlling the shell porosity using MAN.

Supplementary Materials: The following supporting information can be downloaded at: https://www.mdpi.com/article/10.3390/su15032023/s1. Figure S1: The variation of shear stress as a function of shearing strain for co-monomers R1 and R2. The viscosity of R1 and R2 are 0.0042 and 0.0186 Pa.s, respectively. Table S1: The densities and viscosities of the different fluids. Table S2: The experimental parameters and sizes of droplets. σ: the standard deviation; CV: the coefficient of variation. Table S3: Calculation details of the average size of microparticles for experiment E8. Table S4: Calculation details of the average size of microparticles for experiment E9. Table S5: Calculation details of the average size of microparticles for experiment E17. Table S6: Calculation details of the average size of microparticles for experiment E18.

Author Contributions: Conceptualization, H.E.I. and S.F.; methodology, H.E.I., S.F., N.R. and A.Z.; validation, H.E.I. and S.F.; investigation, H.E.I., S.F. and A.Z.; resources, P.P. and F.A.; data curation, H.E.I., W.L. and N.R.; writing—original draft preparation, H.E.I.; writing—review and editing, S.F., A.Z., N.R., P.P. and F.A.; visualization, H.E.I., S.F. and A.Z.; supervision, P.P. and F.A.; project administration, H.E.I. and S.F.; funding acquisition, H.E.I., S.F., P.P. and F.A. All authors have read and agreed to the published version of the manuscript.

Funding: This research was funded by the Federative research structure SFR Condorcet—FR CNRS 3417, grant number 08/2022/SFR/AH.

Institutional Review Board Statement: Not applicable.

Informed Consent Statement: Not applicable.

Data Availability Statement: Not applicable.

Acknowledgments: Communauté urbaine du Grand Reims, Département de la Marne, Région Grand Est and European Union (FEDER Champagne-Ardenne 2014–2020) are acknowledged for their financial support to the Chair of Biotechnology of CentraleSupélec, URD ABI AgroParisTech, and the Centre Européen de Biotechnologie et de Bioéconomie (CEBB).

Conflicts of Interest: The authors declare no conflict of interest.

References

1. Picart, S.; Parant, P.; Caisso, M.; Remy, E.; Mokhtari, H.; Jobelin, I.; Bayle, J.P.; Martin, C.L.; Blanchart, P.; Ayral, A.; et al. Porous Metal Oxide Microspheres from Ion Exchange Resin. *Eur. Phys. J. Spec. Top.* **2015**, *224*, 1675–1687. https://doi.org/10.1140/epjst/e2015-02490-y.
2. Shinde, P.S.; Suryawanshi, P.S.; Patil, K.K.; Belekar, V.M.; Sankpal, S.A.; Delekar, S.D.; Jadhav, S.A. A Brief Overview of Recent Progress in Porous Silica as Catalyst Supports. *J. Compos. Sci.* **2021**, *5*, 75. https://doi.org/10.3390/jcs5030075.
3. Qutachi, O.; Vetsch, J.R.; Gill, D.; Cox, H.; Scurr, D.J.; Hofmann, S.; Müller, R.; Quirk, R.A.; Shakesheff, K.M.; Rahman, C.V. Injectable and Porous PLGA Microspheres That Form Highly Porous Scaffolds at Body Temperature. *Acta Biomater.* **2014**, *10*, 5090–5098. https://doi.org/10.1016/j.actbio.2014.08.015.
4. Cai, Y.; Chen, Y.; Hong, X.; Liu, Z.; Yuan, W. Porous Microsphere and Its Applications. *Int. J. Nanomed.* **2013**, *8*, 1111–1120. https://doi.org/10.2147/IJN.S41271.
5. Nandiyanto, A.B.D.; Ogi, T.; Wang, W.N.; Gradon, L.; Okuyama, K. Template-Assisted Spray-Drying Method for the Fabrication of Porous Particles with Tunable Structures. *Adv. Powder Technol.* **2019**, *30*, 2908–2924. https://doi.org/10.1016/j.apt.2019.08.037.
6. Baldelli, A.; Vehring, R. Control of the Radial Distribution of Chemical Components in Spray-Dried Crystalline Microparticles. *Aerosol Sci. Technol.* **2016**, *50*, 1130–1142. https://doi.org/10.1080/02786826.2016.1216941.
7. Baldelli, A.; Power, R.M.; Miles, R.E.H.; Reid, J.P.; Vehring, R. Effect of Crystallization Kinetics on the Properties of Spray Dried Microparticles. *Aerosol Sci. Technol.* **2016**, *50*, 693–704. https://doi.org/10.1080/02786826.2016.1177163.
8. Yu, Y.; Li, G.; Han, W.; Zhu, L.; Si, T.; Wang, H.; Sun, Y.; He, Y. An Efficient Preparation of Porous Polymeric Microspheres by Solvent Evaporation in Foam Phase. *Chin. J. Chem. Eng.* **2021**, *29*, 409–416. https://doi.org/10.1016/j.cjche.2020.09.002.
9. Chen, S.; Gao, F.; Wang, Q.; Su, Z.; Ma, G. Double Emulsion-Templated Microspheres with Flow-through Pores at Micrometer Scale. *Colloid Polym. Sci.* **2013**, *291*, 117–126. https://doi.org/10.1007/s00396-012-2717-8.
10. Sosnik, A.; Seremeta, K.P. Advantages and Challenges of the Spray-Drying Technology for the Production of Pure Drug Particles and Drug-Loaded Polymeric Carriers. *Adv. Colloid Interface Sci.* **2015**, *223*, 40–54. https://doi.org/10.1016/j.cis.2015.05.003.
11. El Itawi, H.; Fadlallah, S.; Allais, F.; Perré, P. Green Assessment of Polymer Microparticles Production Processes: A Critical Review. *Green Chem.* **2022**, *24*, 4237–4269. https://doi.org/10.1039/d2gc00578f.
12. Brugarolas, T.; Tu, F.; Lee, D. Directed Assembly of Particles Using Microfluidic Droplets and Bubbles. *Soft Matter* **2013**, *9*, 9046–9058. https://doi.org/10.1039/C3SM50888A.
13. Giudice, F.D.; D'Avino, G.; Maffettone, P.L. Microfluidic Formation of Crystal-like Structures. *Lab Chip* **2021**, *21*, 2069–2094. https://doi.org/10.1039/D1LC00144B.
14. Boskovic, D.; Loebbecke, S. Synthesis of Polymer Particles and Capsules Employing Microfluidic Techniques. *Nanotechnol. Rev.* **2013**, *3*, 27–38. https://doi.org/10.1515/ntrev-2013-0014.
15. Xu, Q.; Hashimoto, M.; Dang, T.T.; Hoare, T.; Kohane, D.S.; Whitesides, G.M.; Langer, R.; Anderson, D.G.; David, H. Preparation of Monodisperse Biodegradable Polymer Microparticles Using a Microfluidic Flow-Focusing Device for Controlled Drug Delivery. *Small* **2009**, *5*, 1575–1581. https://doi.org/10.1002/smll.200801855.
16. Zhang, Y.; Cattrall, R.W.; Kolev, S.D. Fast and Environmentally Friendly Microfluidic Technique for the Fabrication of Polymer Microspheres. *Langmuir* **2017**, *33*, 14691–14698. https://doi.org/10.1021/acs.langmuir.7b03574.
17. Busatto, C.A.; Taverna, M.E.; Lescano, M.R.; Zalazar, C.; Estenoz, D.A. Preparation and Characterization of Lignin Microparticles-in-Alginate Beads for Atrazine Controlled Release. *J. Polym. Environ.* **2019**, *27*, 2831–2841. https://doi.org/10.1007/s10924-019-01564-2.
18. Dubinsky, S.; Zhang, H.; Nie, Z.; Gourevich, I.; Voicu, D.; Deetz, M.; Kumacheva, E. Microfluidic Synthesis of Macroporous Copolymer Particles. *Macromolecules* **2008**, *41*, 3555–3561. https://doi.org/10.1021/ma800300d.
19. Xu, S.; Nisisako, T. Polymer Capsules with Tunable Shell Thickness Synthesized via Janus-to-Core Shell Transition of Biphasic Droplets Produced in a Microfluidic Flow-Focusing Device. *Sci. Rep.* **2020**, *10*, 4549. https://doi.org/10.1038/s41598-020-61641-8.
20. Serra, C.A.; Chang, Z. Microfluidic-Assisted Synthesis of Polymer Particles. *Chem. Eng. Technol.* **2008**, *31*, 1099–1115.
21. Nie, Z.; Xu, S.; Seo, M.; Lewis, P.C.; Kumacheva, E. Polymer Particles with Various Shapes and Morphologies Produced in Continuous Microfluidic Reactors. *J. Am. Chem. Soc.* **2005**, *127*, 8058–8063. https://doi.org/10.1021/ja042494w.
22. Zhang, H.; Ju, X.J.; Xie, R.; Cheng, C.J.; Ren, P.W.; Chu, L.Y. A Microfluidic Approach to Fabricate Monodisperse Hollow or Porous Poly(HEMA-MMA) Microspheres Using Single Emulsions as Templates. *J. Colloid Interface Sci.* **2009**, *336*, 235–243. https://doi.org/10.1016/j.jcis.2009.03.070.

23. Kim, C.M.; Ullah, A.; Chang, C.H.; Kim, G.M. Preparation of Lidocaine-Loaded Porous Poly (Lactic-Co-Glycolic Acid) Microparticles Using Microfluidic Flow Focusing and Phosphate Buffer Solution Porogen. *Int. J. Precis. Eng. Manuf.* **2017**, *18*, 599–604. https://doi.org/10.1007/s12541-017-0071-y.
24. Fadlallah, S.; Roy, P.S.; Garnier, G.; Saito, K.; Allais, F. Are Lignin-Derived Monomers and Polymers Truly Sustainable? An in-Depth Green Metrics Calculations Approach. *Green Chem.* **2021**, *23*, 1495–1535.
25. Wang, H.; Pu, Y.; Ragauskas, A.; Yang, B. From Lignin to Valuable Products–Strategies, Challenges, and Prospects. *Bioresour. Technol.* **2019**, *271*, 449–461. https://doi.org/10.1016/j.biortech.2018.09.072.
26. Mao, S.; Zhang, T.; Sun, W.; Ren, X. The Depolymerization of Sodium Alginate by Oxidative Degradation. *Pharm. Dev. Technol.* **2012**, *17*, 763–769. https://doi.org/10.3109/10837450.2011.583927.
27. No, H.K.; Prinyawiwatkul, W. Stability of Chitosan Powder during Long-Term Storage at Room Temperature. *J. Agric. Food Chem.* **2009**, *57*, 8434–8438. https://doi.org/10.1021/jf902012t.
28. Halpern, Y.; Riffer, R.; Broido, A. Levoglucosenone (1,6-Anhydro-3,4-Dideoxy-Δ3-β-D-Pyranosen-2-One). A Major Product of the Acid-Catalyzed Pyrolysis of Cellulose and Related Carbohydrates. *J. Org. Chem.* **1973**, *38*, 204–209. https://doi.org/10.1021/jo00942a005.
29. Fadlallah, S.; Mouterde, L.M.M.; Garnier, G.; Saito, K.; Allais, F. Cellulose-Derived Levoglucosenone, a Great Versatile Chemical Platform for the Production of Renewable Monomers and Polymers. *ACS Symp. Ser.* **2020**, *1373*, 77–97. https://doi.org/10.1021/bk-2020-1373.ch005.
30. Flourat, A.L.; Haudrechy, A.; Allais, F.; Renault, J.H. (S)-γ-Hydroxymethyl-α,β-Butenolide, a Valuable Chiral Synthon: Syntheses, Reactivity, and Applications. *Org. Process Res. Dev.* **2020**, *24*, 615–636. https://doi.org/10.1021/acs.oprd.9b00468.
31. Krishna, S.H.; McClelland, D.J.; Rashke, Q.A.; Dumesic, J.A.; Huber, G.W. Hydrogenation of Levoglucosenone to Renewable Chemicals. *Green Chem.* **2017**, *19*, 1278–1285. https://doi.org/10.1039/c6gc03028a.
32. Mouterde, L.M.M.; Allais, F.; Stewart, J.D. Enzymatic Reduction of Levoglucosenone by an Alkene Reductase (OYE 2.6): A Sustainable Metal- and Dihydrogen-Free Access to the Bio-Based Solvent Cyrene®. *Green Chem.* **2018**, *20*, 5528–5532. https://doi.org/10.1039/C8GC03146K.
33. Sherwood, J.; De bruyn, M.; Constantinou, A.; Moity, L.; McElroy, C.R.; Farmer, T.J.; Duncan, T.; Raverty, W.; Hunt, A.J.; Clark, J.H. Dihydrolevoglucosenone (Cyrene) as a Bio-Based Alternative for Dipolar Aprotic Solvents. *Chem. Commun.* **2014**, *50*, 9650–9652. https://doi.org/10.1039/c4cc04133j.
34. Camp, J.E. Bio-Available Solvent Cyrene: Synthesis, Derivatization, and Applications. *ChemSusChem* **2018**, *11*, 3048–3055. https://doi.org/10.1002/cssc.201801420.
35. Guajardo, N.; Domínguez de María, P. Assessing Biocatalysis Using Dihydrolevoglucosenone (Cyrene™) as Versatile Bio-Based (Co)Solvent. *Mol. Catal.* **2020**, *485*, 110813. https://doi.org/10.1016/j.mcat.2020.110813.
36. Duval, A.; Avérous, L. Dihydrolevoglucosenone (Cyrene™) as a Versatile Biobased Solvent for Lignin Fractionation, Processing, and Chemistry. *Green Chem.* **2022**, *24*, 338–349. https://doi.org/10.1039/D1GC03395F.
37. Bai, Y.; Hawley, W.B.; Jafta, C.J.; Muralidharan, N.; Polzin, B.J.; Belharouak, I. Sustainable Recycling of Cathode Scraps via Cyrene-Based Separation. *Sustain. Mater. Technol.* **2020**, *25*, e00202. https://doi.org/10.1016/j.susmat.2020.e00202.
38. Kumar, S.; Ignacz, G.; Szekely, G. Synthesis of Covalent Organic Frameworks Using Sustainable Solvents and Machine Learning. *Green Chem.* **2021**, *23*, 8932–8939. https://doi.org/10.1039/D1GC02796D.
39. Vastano, M.; Pellis, A.; Botelho Machado, C.; Simister, R.; McQueen-Mason, S.J.; Farmer, T.J.; Gomez, L.D. Sustainable Galactarate-Based Polymers: Multi-Enzymatic Production of Pectin-Derived Polyesters. *Macromol. Rapid Commun.* **2019**, *40*, 1900361. https://doi.org/10.1002/marc.201900361.
40. Fadlallah, S.; Peru, A.A.M.; Longé, L.; Allais, F. Chemo-Enzymatic Synthesis of a Levoglucosenone-Derived Bi-Functional Monomer and Its Ring-Opening Metathesis Polymerization in the Green Solvent Cyrene™. *Polym. Chem.* **2020**, *11*, 7471–7475. https://doi.org/10.1039/D0PY01471K.
41. Ray, P.; Hughes, T.; Smith, C.; Hibbert, M.; Saito, K.; Simon, G.P. Development of Bio-Acrylic Polymers from Cyrene™: Transforming a Green Solvent to a Green Polymer. *Polym. Chem.* **2019**, *10*, 3334–3341. https://doi.org/10.1039/C9PY00353C.
42. Sreenivasaya, M.; Pirie, N.W. The Disintegration of Tobacco Mosaic Virus Preparations with Sodium Dodecyl Sulphate. *Biochem. J.* **1938**, *32*, 1707–1710. https://doi.org/10.1042/bj0321707.
43. Kiatkamjornwong, S.; Chientachakul, P.; Prasassarakich, P.; Damronglerd, S. Kinetic Studies on Styrene-Divinylbenzene Copolymerization by Suspension Technique. *J. Appl. Polym. Sci.* **2001**, *82*, 1521–1540. https://doi.org/10.1002/app.1991.
44. Meister, B.J.; Scheele, G.F. Prediction of Jet Length in Immiscible Liquid Systems. *AIChE J.* **1969**, *15*, 689–699. https://doi.org/10.1002/aic.690150512.
45. Zhang, D.F.; Stone, H.A. Drop Formation in Viscous Flows at a Vertical Capillary Tube. *Phys. Fluids* **1997**, *9*, 2234–2242.
46. Prat, D.; Wells, A.; Hayler, J.; Sneddon, H.; McElroy, C.R.; Abou-Shehada, S.; Dunn, P.J. CHEM21 Selection Guide of Classical- and Less Classical-Solvents. *Green Chem.* **2015**, *18*, 288–296. https://doi.org/10.1039/c5gc01008j.